





# Photoacoustic imaging of hemodynamic changes in forearm skeletal muscle during cuff occlusion

JINGE YANG,<sup>1</sup>  GUANG ZHANG,<sup>2,3</sup> WU CHANG,<sup>2,3</sup> ZIHUI CHI,<sup>1</sup>  
QIQUAN SHANG,<sup>2,3</sup>  MAN WU,<sup>2,3</sup> TENG PAN,<sup>2,3</sup> LIN HUANG,<sup>2,3</sup>  
AND HUABEI JIANG<sup>4,\*</sup>

<sup>1</sup>*School of Optoelectric Engineering, Chongqing University of Posts and Telecommunications, Chongqing 400065, China*

<sup>2</sup>*School of Electronic Science and Engineering (National Exemplary School of Microelectronics), University of Electronic Science and Technology of China, Chengdu 611731, China*

<sup>3</sup>*Center for Information in Medicine, University of Electronic and Technology of China, Chengdu 611731, China*

<sup>4</sup>*Department of Medical Engineering, University of South Florida, Tampa 33620, USA*

\**hjiang1@usf.edu*

**Abstract:** Characterizations of circulatory and metabolic function in skeletal muscle are of great importance in clinical settings. Here in this study, we investigate the utility of photoacoustic tomography (PAT) to monitor the hemodynamic changes in forearm skeletal muscle during cuff occlusion. We show high quality photoacoustic (PA) images of human forearm in comparison with ultrasound images. Besides, we track the hemodynamic changes in the forearm during cuff occlusion cross-validated with near-infrared spectroscopy. Our study suggests that PAT, as a new tool, could be applied to common diseases affecting skeletal muscle in the future.

© 2020 Optical Society of America under the terms of the [OSA Open Access Publishing Agreement](#)

## 1. Introduction

Assessment of hemodynamic parameters in skeletal muscle plays an important role in clinical applications [1–5] and provides key information for understanding many diseases affecting skeletal muscle [6–13] such as peripheral vascular disease, heart failure, and Becker muscular dystrophy. No obvious differences can be observed between healthy and muscle diseased populations at resting state, so it is necessary to study muscle hemodynamic in response to stimuli [14–16].

Noninvasive techniques have been developed for examining muscle over the years. Conventional venous occlusion strain gauge plethysmography (SGP), a relative simple technique, has been employed for many years in muscle perfusion [17,18]. However, SGP cannot provide regional information or spatial images. Ultrasound Doppler is widely used as a clinical tool to assess blood flow in large vessels [19,20]. But it is not sensitive to the flow in smaller vessels, and thus it cannot offer hemodynamic changes in muscle. Magnetic resonance imaging (MRI) has high spatial resolution [21,22], but it poses a large financial burden with poor mobility. Positron emission tomography (PET) is also costly and bulky, and has poor spatiotemporal resolution [23,24].

Near-infrared optical techniques including near-infrared spectroscopy (NIRS) and diffuse correlation spectroscopy (DCS) have been used to study muscle physiology and vascular diseases [5,16,25,26]. These techniques enable the sensing of oxy- and deoxy-hemoglobin (HbO<sub>2</sub> and HbR) that are essential tissue indicators of oxygen utilization, metabolism, and muscle function. These methods have improved the quantification of oxygenation levels [27], but their spatial resolution is relatively low.

Photoacoustic tomography is an emerging biomedical method based on the photoacoustic (PA) effect [28]. In PAT, ultrasound signals generated from tissue thermally expanded by laser pulses are used to reconstruct images [29–31]. To date, a PAT system can be offered in a cost-effective and portable manner [27,32–35]. Previous multispectral PAT studies have shown its ability to detect breast cancer [36,37] and thyroid cancer [38,39], perform vascular examination [40,41], probe inflammation [42,43], and image peripheral vasculature [44–46], prostate [47,48] uterine [49], exercised muscle oxygenation [27,50] and flow-mediated dilatation test [51].

It is also noted that blood circulation in the forearm has been visualized with photoacoustic microscopy (PAM) [50,52]. However, these previous studies paid no attention to skeletal muscle.

The purpose of this work is to show the feasibility of PAT for measuring the hemodynamic changes in the forearm muscle during cuff occlusion. We present high resolution PAT images cross-verified by ultrasound images. We also assess the hemodynamic changes and measure multiple hemodynamic parameters in muscle, which are cross-validated with NIRS.

## 2. Methods

### 2.1. Imaging system

For monitoring a subject during the arm-cuff occlusion trial, we utilized a home-made photoacoustic imaging system. The setup is displayed in Fig. 1(a). In this PAT system, the light illumination is provided by a tunable pulsed laser (Surelite OPO, Continuum, CA, USA). The pulse duration is  $\sim 4$  ns and the repetition rate is 20 Hz with a working wavelength range from 720–2500 nm. The maximum fluence at 760 nm was approximately  $18 \text{ mJ/cm}^2$  during the experimentation.

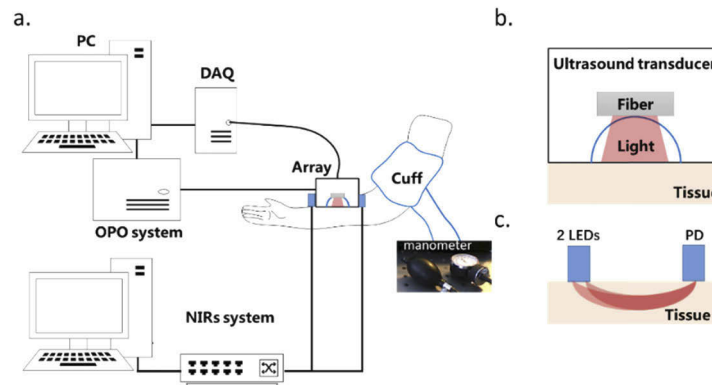


**Fig. 1.** A schematic of the experimental system. (a) The hardware components employed in the PAT system and NIRS system. **DAQ:** Data Acquisition System (preamplifiers, multiplexers and analog-to-digital converters). **OPO:** optical parametric oscillator; **PC:** personal computer; **NIRS system:** data acquisition system for NIRS. (b) Detail of the imaging probe. It contained a 128-element transducer array, a fiber bundle and a resin shell enclosed with a PDMS film. (c) The LEDs and PD were placed at the same region of interest as the PAT probe at an interval of 2 cm.

A custom-made fiber bundle with line-shaped illumination pattern ( $40 \times 2 \text{ mm}^2$ ) was applied to deliver the light from a pulsed laser. The imaging probe, shown in Fig. 1(b), contained a 128-element ultrasound transducer array (a combination of two 5K0.95  $\times$  151–64H, Japan probe, Japan). The elements were arranged in a half arc spanning  $174^\circ$ . The diameter of the transducer was 100 mm and the central frequency was about 5 MHz (90% bandwidth). The imaging probe was fully enclosed with a  $100 \mu\text{m}$  polydimethylsiloxane (PDMS) film which was optically and

acoustically transparent. The cavity between the array and forearm was filled with deionized water for acoustic coupling (Fig. 1(b)).

A custom-built 128-channel preamplifier was connected to the probe, and the amplified PA signals were transferred to a 64-channel analog-to-digital system at a sampling rate of 50 MS/s and 12-bit digital resolution after 2:1 multiplexing (PXIe5105, National Instrument, USA). One computer worked as control panels for the PAT system and saved the PA signal data. One complete frame of data from single wavelength was acquired in 0.5s for the PA signals were averaged for 5 times.

In the NIRS module (Fig. 1(a)), two LEDs (780 nm and 840 nm) were employed to support continues-wave light illumination, and the scattered light emerging at tissue was detected by a photodiode detector (Fig.1c). The light source and detector were arranged in an elastic band at a distance of 2 cm attached to the arm by an elastic band. The data acquisition system adopted a 16-channel, 16-bit data acquisition card PXIe-6358 (National Instrument, USA) with a sampling rate of 1.25 MS/s, which was installed in the PXIe-1073 (National Instrument, USA) chassis to realize the communication between the acquisition card and the control host. The NIRS measurement was performed separately after the PAT imaging was completed each time for the same region of interest in the forearm.

## 2.2. Subjects and protocols

Six healthy adult volunteers (3 men and 3 women, age =  $25 \pm 3$ ) participated in this study. The study was approved by the ethics committee at Chongqing University of Posts and Telecommunications. In an experiment, a subject sat on a chair and laid his/her arm on a comfortable plastic plate. The room temperature was set to 25°C. The imaging probe was placed by a mechanical arm over the right forearm at one position 30 mm from the elbow to the hand side. A blood pressure cuff was placed around the right upper arm. Two cuff occlusion trials were carried out in series for PAT and NIRS.

One whole trial lasted for 10 minutes, and before the trial rest state images were obtained at two wavelengths (760 nm and 840 nm). Dynamic changes which reflect the blood perfusion during the PA trial were imaged at 800 nm which is the isosbestic point in the hemoglobin absorption spectrum. Images at this wavelength are not affected by changes in the content of oxy- and deoxygenated hemoglobin in blood vessels and muscle region. We obtained PA images in the first 2 minutes as the baseline data. Then 2 minutes venous occlusion (VO) was applied to the subject. The pressure cuff was inflated to 80 mm Hg during the occlusion. After the VO, the pressure was rapidly released and there was a 2 minutes rest between two occlusions. Then the second occlusion arterial occlusion (AO) was applied with 180mm Hg pressure inflated in the cuff, held for another 2 minutes, and then released. The measurement was made during the recovery period for 2 minutes. The same occlusion trials were conducted using NIRS 10 minutes after the PAT imaging.

## 2.3. Reconstruction method and data analysis

Before the reconstruction, PA signals were processed by a bandpass filter (0.2–5 MHz) to remove the high-frequency noise. PA images were reconstructed by using a universal back-projection reconstruction algorithm [53] and were registered to the first frame through a transformation package in Matlab (Mathworks, Inc., MA, USA). Based on these images at 2 different wavelengths and the dynamic changes during occlusion trail, we derived some main physiological properties of the tissue as follows:

Oxygen saturation (SO<sub>2</sub>) and total hemoglobin (HbT): In PA imaging, the multispectral acquisitions were further unmixed to retrieve the distribution of oxygenated (HbO<sub>2</sub>) and deoxygenated (HbR) hemoglobin [31,43,54,55]. This was achieved by least squares spectral fitting of individual pixels reconstructed at the two different wavelengths to the molar extinction spectra of HbO<sub>2</sub>

and HbR. Oxygen saturation ( $SO_2$ ) mapping was calculated as  $SO_2 = HbO_2/(HbO_2+HbR)$ . Total hemoglobin (HbT) changes, which reflect the blood perfusion, were measured by 800 nm during occlusion as 800 nm is the isosbestic point of Hb and HbO<sub>2</sub>.

The temporal changes in HbT and  $SO_2$  in rest state obtained in NIRS measurements were calculated via the well-known semi-infinite medium modified Beer-Lambert law [5,11].

Characterization of responses: To characterize hemodynamic responses in muscle tissue during VO, mean and standard deviation (SD) were tabulated for averaged  $SO_2$ , and blood flow (BF) which is similar to previous studies [5]. The BF can be calculated because during the VO, venous outflow draining the tissue is reduced to zero but the inflow of the arterial is unaltered [3,5,25]. So there is no outflow but constant inflow which caused a linear increase in the concentration of HbT ([HbT]) with a constant rate. We measured the BF during occlusion which is proportional to the rate of increase in blood volume as follows [56]:

$$BF = \frac{1}{c} \frac{d[HbT]}{dt} \quad (1)$$

where  $c$  is the concentration of hemoglobin in the blood, which is assumed or is measured from a blood gas sample. Similar to previous studies [3], we assumed  $c$  to be 14.1 g/dL. The BF was determined from the slope of HbT during the temporal interval  $[T_{fit}(s)]$  where the rate of increase was linear as shown in Fig. 4.

### 3. Results

#### 3.1. PAT and US images of the forearm

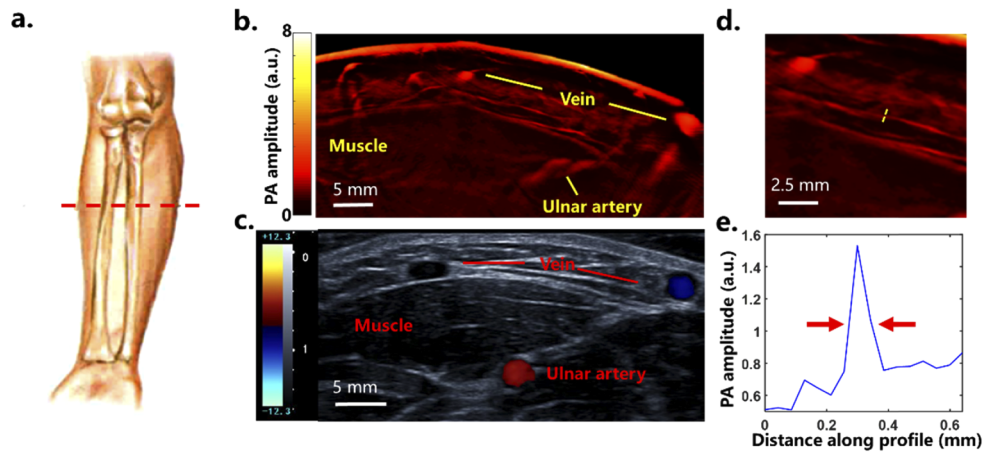
Figure 2 shows a side-by-side comparison between an anatomical cross-sectional US image (iNSIGHT 23R, Saset Healthcare, Inc. Chengdu, China) and a PAT image (800 nm) at rest state before the trial. A layer of strong signal from the skin with an underlying layer of adipose tissue with low PA signal appeared here. Below the adipose region, layers of small blood vessels were observed in the PA images which were not visualized in the US images. Because of the low scattering of ultrasound waves, the in-plane resolution of our PA images system is about  $\sim 150$   $\mu\text{m}$  in theory [29,35]. One small vessel was selected to measure the resolution of our PA images labeled by yellow dashed line in Fig. 2(d). The PA amplitude distribution along the yellow dashed line showed that the full width at half maximum (FWHM) of the profile was about 150  $\mu\text{m}$  shown in Fig. 2(e).

For better coupling of ultrasound signal in both the PAT and US, the imaging probe was pressed against the muscle, and so some superficial veins were squished. The flexor carpi ulnaris muscle could be seen clearly in both the PAT and US images with a sharp margin. The ulnar artery was detected in the PAT image about 10 mm in depth below the skin. Anatomically, the information provided by the PAT image was in agreement with the stratified anatomy of the human forearm US image. The high PAT image quality allowed us to trace the hemodynamic changes in different tissues during occlusion.

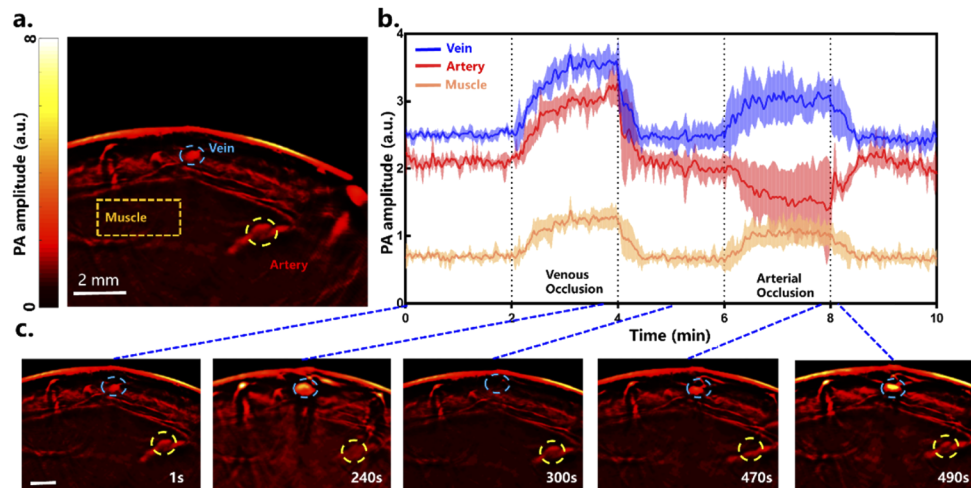
#### 3.2. Hemodynamic changes

Figure 3 shows a sequence of images overtime during the occlusion trial acquired at 800 nm laser illumination. These profiles (Fig. 3(b)) illustrate PA signal changes at three ROIs, namely, a superficial vein (vein), the flexor carpi ulnaris muscle (muscle) and the ulnar artery (artery) (see Fig. 3(a)). Figure 3(b) shows the PA signal profiles from three ROIs over the entire acquisition window in 10 minutes. Figure 3(c) shows subsequent images overtime during the occlusion.

The first occlusion began at 120 s and lasted for 2 minutes. A tendency to saturation in the muscle, vein and artery was observed. The venous outflow was blocked while the arterial inflow remained unaltered. Thus, the concentration of HbT (or blood volume) achieved a saturation



**Fig. 2.** Imaging location and corresponding PAT and US images. (a) Netter's anatomy of human forearm showing the imaging location, indicated by a red dashed line. (b) Cross-sectional PAT image of the imaging location. a.u.=arbitrary unit (c) Corresponding US image of the same location. (d) One small vessel was selected (yellow dashed line) to measure the PAT resolution. (e) Photoacoustic signal profile along the yellow dashed line showing the full width at half maximum to be about 150  $\mu\text{m}$ .



**Fig. 3.** Dynamic changes within the cross-sectional PA images during the trial. (a) Reference PAT image at 800 nm where three regions of interest (ROIs) were selected. (b) Temporal PA signal trace during the occlusion trial (reported as mean  $\pm$  SD). (c) A series of close-up PAT images at different time points show the dimensional changes of a vein and the ulnar artery. a.u.=arbitrary unit

state causing a significant rise in PA signal in the three ROIs as well as a change in the size of the vein and artery.

The dilation of the vein under the skin (Fig. 3(c)) was observed, and HbT increased during VO. No time delay was noted in the three ROIs but the changes in the PA signal were significantly higher in the artery and vein compared to that in the muscle. Following the release of occlusion, the PA signals dropped to the initial baseline values.



After 2 minutes of resting, AO was applied for another 2 minutes and different responses to AO were shown among the three regions. PA signals in muscle and vein rapidly increased to a maximum value while the signal in the artery fell to a stable state along with a change in the size of the ulnar artery.

When the occlusion was released, there was reactive hyperemia because of the auto-regulation of muscle and vessels in response to metabolites during ischemia. As a result, we observed a transient increase in PA signal in the artery and drops in vein and muscle.

### 3.3. Cuff occlusion response in muscle between PAT and NIRS

Here we compare the PA and NIRS responses during VO as shown in Fig. 4 from the muscle ROI. The characteristics of responses during VO are further compared and listed in Table 1. It is known that calculating the absolute [HbT] using PAT in deep tissue is challenging [29] which needs more studies in the future, so we set a scale factor (10 times) to scale up our PA signal as we assumed that the maximum mean signal change of PA signal (0.63) and HbT concentration change (6.21) were similar for the same subject. Our results were comparable to the [HbT] change measured by NIRS and by other optical methods [5,16] as shown in Table 1.

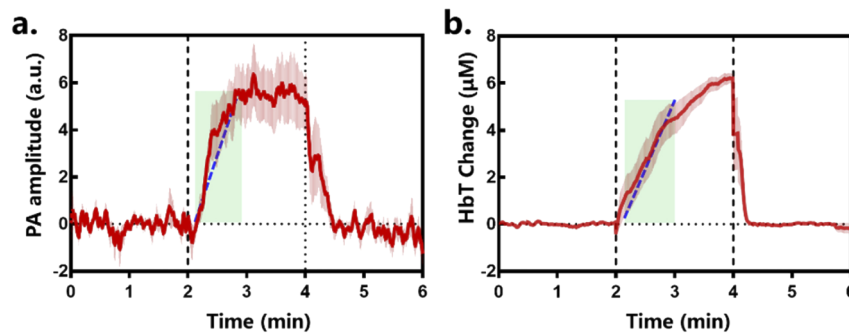


**Fig. 4.** Temporal PA signal (a) and [HbT] trace (b) by NIRS during VO measurements from 6 volunteers from the muscle ROI. The results are reported as mean  $\pm$  SD.  $T_{\text{fit}}$ (s) is the time interval (shaded green region) used for the linear regression fit of PA signal or [HbT] change (blue dashed line) during venous occlusion (VO).

**Table 1.** Comparison of the PAT hemodynamic measurements with NIRS and other optical methods reported in refs.5 and 28. The results are reported as mean  $\pm$  SD.

Method	Static $\text{SO}_2$ (%)	Blood flow( $\text{ml}\cdot 100\text{ml}^{-1}\cdot \text{min}^{-1}$ )
NIRS	$58.2 \pm 4.38$	$1.41 \pm 0.43$
PA	$54.9 \pm 1.12$	$1.75 \pm 0.42$
Ref. [5,28]	$57.8 \pm 7.55$	$1.56 \pm 0.54$

Cuff occlusion of the arm produced similar responses among volunteers using the two methods. PA signal showed higher standard deviation and lower maximum PA signal change at the end of the 2 minutes VO compared to NIRS. During the VO, the blood flow measured by PAT ( $1.75 \pm 0.42$ ) was close to that by NIRS ( $1.41 \pm 0.43$ ) and the other references ( $1.56 \pm 0.54$ ). The static  $\text{SO}_2$  by PAT was  $54.9 \pm 1.12\%$  compared to that by NIRS ( $58.2 \pm 4.38\%$ ) and that by other optical methods ( $57.8 \pm 7.55\%$ ).

## 4. Discussion

Assessing the blood oxygenation level and hemodynamic changes in the muscle are of importance in clinical applications [1–5]. It has been investigated with multiple modalities including MRI, NIRS, ultrasound Doppler, PET and SPG [17–24]. Data obtained from these modalities represent different types of physiological signals and are affected by different artifacts. In this study, by taking advantage of PAT, we showed that PAT is efficient for tracing hemodynamic changes during cuff occlusion, and can accurately resolve the signals among different depths/layers in muscle with high resolution.

### 4.1. PAT imaging for deep tissue

Taking advantage of different optical absorptions among different tissues, we could differentiate the upper layers including skin surface, adipose tissue, vein, muscle and artery. The thickness of the upper layers above the flexor carpi ulnaris muscle is about  $2.3 \pm 0.3$  mm according to the PAT images. The ulnar artery, which plays a critical role in the circulation system in the forearm, was observed here in both the PAT and US images.

Anatomically, the information provided by PAT images was in agreement with the stratified anatomy of the human forearm images from US. With deep penetration and high resolution, we segmented different tissues for further studies based on their optical absorptions without an advanced segmentation algorithm and showed the hemodynamic changes in response to cuff occlusion.

### 4.2. Healthy subject responses

Based on our PAT images, we demonstrated the hemodynamic responses in forearm during cuff occlusion for six healthy volunteers. Before the occlusion, blood volume in different tissues was relatively stable resulting in stable PA signal and [HbT]. During the VO, the venous outflow was blocked while the arterial inflow remained unaltered, and so blood volume increased to a saturation state in the muscle, vein and artery causing significant PA signal and [HbT] changes.

The outflow of blood entered into blocked veins, leading to a saturated [HbT] in the entire region (vein, artery and muscle). Because of a varying degree of auto-regulatory behavior [57], changes in muscle were not as sharp as in vessels.

When the vasculature in muscle approached maximal dilation, the venous blood pressure increased. The dilation of vein under the skin (Fig. 3(c)) and increased HbT were observed during VO. The blood pressure increases in veins and muscle reduced the arterial inflow, and hence HbT started to level off toward a saturation state as arterial inflow dropped to zero. It seemed that it took about 1 minute to allow complete saturation. After the release of the cuff, the PA signal and [HbT] dropped to the baseline.

We noticed that at the onset of the venous occlusion, the increase in HbT was nonlinear because it needed about 3–5 s to inflate the cuff. Then it settled to a steady rate of increase at full cuff inflation which allowed us to calculate the BF during the VO. The first 3–5 s during VO were not included in the computation of BF.

At the onset of the AO, different responses were shown among the muscle, veins and artery. It needed about 10–15 s to inflate the cuff to raise the cuff pressure above the artery pressure, and since the associated VO hinders the outflow, a transient signal increase was observed in the vein and muscle. At the same time, PA signal in artery decreased with the collapse of blood vessels. Once the artery was totally blocked, the inflow and outflow decreased to zero while the HbT concentration remained unchanged until the release of the AO. This stable state measured by HbT during cuff occlusion might be related to the so-called “biological zero” [58] for AO blocked both the artery and vein, and the inflow and outflow of this region were reduced to zero.

When the occlusion was released, there was reactive hyperemia because of the auto-regulation (vasodilation) of muscle and vessels in response to metabolites during ischemia [16]. As a result, we observed a transient increase in HbT in artery to baseline.

#### 4.3. Comparison of responses with NIRS

Similar responses in  $SO_2$  and other hemodynamic parameters before occlusion were observed among PAT, NIRS and other optical methods. However, we note that lower  $SO_2$  and higher BF were seen in PAT.

The differences between PAT and NIRS data may be due to the re-localization of NIRS sensors as PAT and NIRS data were not acquired simultaneously. The distance of LEDs and PDs varied from person to person slightly, which might change the light path length resulting in errors in NIRS [3,62] while the imaging probe for PAT was fixed in position. Further, although the illumination/imaging area was marked during the PAT, slight movement of the NIRS sensors might also cause some errors as the skin/muscle are deformable.

PA signal from the muscle reflected only the local response to occlusion as we could select the muscle as ROI among other tissues which cannot be distinguished by NIRS and other optical methods. Moreover, the least square method as a linear un-mixing method used in this study, does not consider the spatially varying wavelength-dependence of the light fluence in biological tissue [63]. Distorted photoacoustic spectrum, which is known as “spectral coloring” can introduce significant inaccuracies in the estimation of blood oxygenation [64].

## 5. Conclusions

We have shown that photoacoustic tomography can be used to study physiological parameters during cuff occlusion trials with high spatial resolution. We visualized the reaction of muscle and vessels in the forearm during occlusion and analyzed the hemodynamic fluctuations. We demonstrated the HbT changes during occlusion and computed the BF by PAT and compared our PAT findings with NIRS and other optical studies with good correlation for the first time.

We realize that there are some limitations associated with our present PAT system. Compared to NIRS, the PAT system is expensive and cumbersome. This might be resolved by a compact laser system [35,59] with a lower price and portable configuration. In addition, a fast tuning OPO system might be applied in a future study to help us trace the  $SO_2$  change during the occlusion.

Moreover, calculations of hemodynamic parameters and  $SO_2$  are important in physiological studies and the accuracy of the computation needs to be improved. Establishing appropriate computational models by the finite element method [60] and separating the different components such as myoglobin using more wavelengths [61] may help.

Overall, we expect that PAT has the potential to become a clinical tool in applications especially related to physical therapy and gene therapy, where monitoring of blood oxygenation level in the muscle is of importance [1]. The high resolution PAT images allow improved measurements of specific tissue components by computing signals from accurately defined volumes.

## Funding

National Natural Science Foundation of China (61701076).

## Disclosures

The authors declare no conflicts of interest.

## References

1. T. Hamaoka, K. K. McCully, M. Niwayama, and B. Chance, “The use of muscle near-infrared spectroscopy in sport, health and medical sciences: recent developments,” *Philos. Trans. R. Soc., A* **369**(1955), 4591–4604 (2011).



2. H. T. McCully K K, "Near-infrared spectroscopy: What can it tell us about oxygen saturation in skeletal," *Exerc. Sport. Sci. Rev.* **28**(3), 123–127 (2000).
3. K. Gurley, Y. Shang, and G. Yu, "Noninvasive optical quantification of absolute blood flow, blood oxygenation, and oxygen consumption rate in exercising skeletal muscle," *J. Biomed. Opt.* **17**(7), 0750101 (2012).
4. R. C. Mesquita, T. Durduran, G. Yu, E. M. Buckley, M. N. Kim, C. Zhou, R. Choe, U. Sunar, and A. G. Yodh, "Direct measurement of tissue blood flow and metabolism with diffuse optics," *Philos. Trans. R. Soc., A* **369**(1955), 4390–4406 (2011).
5. Z. Li, W. Baker, A. Parthasarathy, T. Ko, D. Wang, S. Schenkel, T. Durduran, G. Li, and A. Yodh, "Calibration of diffuse correlation spectroscopy blood flow index with venous-occlusion diffuse optical spectroscopy in skeletal muscle," *J. Biomed. Opt.* **20**(12), 125005 (2015).
6. K. Ouriel, "Peripheral arterial disease," *Lancet* **358**(9289), 1257–1264 (2001).
7. T. R. Cheattle, L. A. Potter, M. Cope, D. T. Delpy, and J. H. Scurr, "Near-infrared spectroscopy in peripheral vascular disease," *Br. J. Surg.* **78**(4), 405–408 (1991).
8. U. Wolf, M. Wolf, J. H. Choi, M. Levi, D. Choudhury, S. Hull, D. Coussirat, L. A. Paunescu, L. P. Safonova, A. Michalos, W. W. Mantulin, and E. Gratton, "Localized irregularities in hemoglobin flow and oxygenation in calf muscle in patients with peripheral vascular disease detected with near-infrared spectrophotometry," *J. Vasc. Surg-Venous L.* **37**(5), 1017–1026 (2003).
9. A. Elvin, A. K. Siösteen, A. Nilsson, and E. Kosek, "Decreased muscle blood flow in fibromyalgia patients during standardised muscle exercise: A contrast media enhanced colour doppler study," *Eur. J. Pain.* **10**(2), 137 (2006).
10. J. M. Arnold, J. P. Ribeiro, and W. S. Colucci, "Muscle blood flow during forearm exercise in patients with severe heart failure," *Circulation* **82**(2), 465–472 (1990).
11. T. Y. Abay and P. A. Kyriacou, "Comparison of NIRS, laser Doppler flowmetry, photoplethysmography, and pulse oximetry during vascular occlusion challenges," *Physiol. Meas.* **37**(4), 503–514 (2016).
12. A. Lima and J. Bakker, "Noninvasive monitoring of peripheral perfusion," *Intensive Care Med.* **31**(10), 1316–1326 (2005).
13. Y. Sakr, "Techniques to assess tissue oxygenation in the clinical setting," *Transfus. Apher. Sci.* **43**(1), 79–94 (2010).
14. J. L. Jasperse, D. R. Seals, and R. Callister, "Active forearm blood flow adjustments to handgrip exercise in young and older healthy men," *J. Physiol. Paris* **474**(2), 353–360 (1994).
15. K. K. McCully, C. Halber, and J. D. Posner, "Exercise-induced changes in oxygen saturation in the calf muscles of elderly subjects with peripheral vascular disease," *J. Gerontol.* **49**(3), B128–B134 (1994).
16. G. Yu, T. Durduran, G. Lech, C. Zhou, and A. G. Yodh, "Time-dependent blood flow and oxygenation in human skeletal muscles measured by noninvasive near-infrared diffuse optical spectroscopies," *J. Biomed. Opt.* **10**(2), 024027 (2005).
17. R. J. Whitney, "The measurement of volume changes in human limbs," *J. Physiol. Paris.* **121**(1), 1–27 (1953).
18. K. A. Engelke, J. R. Halliwill, D. N. Proctor, N. M. Dietz, and M. J. Joyner, "Contribution of nitric oxide and prostaglandins to reactive hyperemia in the human forearm," *J. Appl. Physiol.* **81**(4), 1807–1814 (1996).
19. J. R. Libonati, A. K. Howell, N. M. Incanno, K. K. Pettee, and H. L. Glassberg, "Brief Muscle Hypoperfusion/Hyperemia: An Ergogenic Aid?" *J. Strength Cond. Res* **15**(3), 362–366(2001).
20. J. R. Libonati, M. Cox, N. Incanno, S. K. Melville, F. C. Musante, H. L. Glassberg, and M. Guazzi, "Brief periods of occlusion and reperfusion increase skeletal muscle force output in humans," *Cardiologia* **43**(12), 1355–1360 (1998).
21. R. S. Richardson, E. A. Noyszewski, L. J. Haseler, S. Bluml, and L. R. Frank, "Evolving techniques for the investigation of muscle bioenergetics and oxygenation," *Biochem. Soc. Trans.* **30**(2), 232–237 (2002).
22. M. K. Peter Schmitt, A. Tobermann, A. Haase, and M. Flentje, "Quantitative tissue perfusion measurements in head and neck carcinoma patients before and during radiation therapy with a non-invasive MR imaging spin-labeling technique," *Radiother. Oncol.* **67**(1), 27–34 (2003).
23. W. Burchert, S. Schellong, J. V. D. Hoff, G. J. Meyer, and H. Hundeshagen, "Oxygen-15-water PET assessment of muscular blood flow in peripheral vascular disease," *J. Nucl. Med.* **38**(1), 93–98 (1997).
24. A. Drzezga, M. Souvatzoglou, M. Eiber, A. J. Beer, S. Furst, A. Martinez-Moller, S. G. Nekolla, S. Ziegler, C. Ganter, and E. J. Rummeny, "First Clinical Experience with Integrated Whole-Body PET/MR: Comparison to PET/CT in Patients with Oncologic Diagnoses," *J. Nucl. Med.* **53**(6), 845–855 (2012).
25. A. D. Edwards, "Measurement of hemoglobin flow and blood flow by near-infrared spectroscopy," *J. Appl. Physiol.* **75**(4), 1884–1889 (1993).
26. M. C. P. V. Beekvelt, W. N. J. M. Colier, R. A. Wevers, and B. G. M. V. Engelen, "Performance of near-infrared spectroscopy in measuring local O<sub>2</sub> consumption and blood flow in skeletal muscle," *J. Appl. Physiol.* **90**(2), 511–519 (2001).
27. G. Diot, A. Dima, and V. Ntziachristos, "Multispectral opto-acoustic tomography of exercised muscle oxygenation," *Opt. Lett.* **40**(7), 1496–1499 (2015).
28. W. Choi, E. Y. Park, S. Jeon, and C. Kim, "Clinical photoacoustic imaging platforms," *Open Biomed. Eng. Lett.* **8**(2), 139–155 (2018).
29. L. V. Wang and S. Hu, "Photoacoustic Tomography: In Vivo Imaging from Organelles to Organs," *Science* **335**(6075), 1458–1462 (2012).
30. Q. Zhang, Z. Liu, P. R. Carney, Z. Yuan, and H. Jiang, "Non-invasive imaging of epileptic seizures in vivo using photoacoustic tomography," *Phys. Med. Biol.* **53**(7), 1921–1931 (2008).

31. J. Yang, D. Wu, G. Zhang, Y. Zhao, and H. Jiang, "Intracerebral haemorrhage-induced injury progression assessed by cross-sectional photoacoustic tomography," *Biomed. Opt. Express* **8**(12), 5814–5824 (2017).
32. X. Luís Deán-Ben and D. Razansky, "Adding fifth dimension to optoacoustic imaging: volumetric time-resolved spectrally enriched tomography," *Light: Sci. Appl.* **3**(1), e137 (2014).
33. X. L. Deán-Ben, E. Merčep, and D. Razansky, "Hybrid-array-based optoacoustic and ultrasound (OPUS) imaging of biological tissues," *Appl. Phys. Lett.* **110**(20), 203703 (2017).
34. A. Buehler, M. Kacprowicz, A. Taruttis, and V. Ntziachristos, "Real-time handheld multispectral optoacoustic imaging," *Opt. Lett.* **38**(9), 1404–1406 (2013).
35. D. Wang, Y. Wang, W. Wang, D. Luo, U. Chitgupi, J. Geng, Y. Zhou, L. Wang, J. F. Lovell, and J. Xia, "Deep tissue photoacoustic computed tomography with a fast and compact laser system," *Biomed. Opt. Express* **8**(1), 112–123 (2017).
36. L. Xi, X. Li, L. Yao, S. Grobmyer, and H. Jiang, "Design and evaluation of a hybrid photoacoustic tomography and diffuse optical tomography system for breast cancer detection," *Med. Phys.* **39**(5), 2584–2594 (2012).
37. E. I. Neuschler, R. Butler, C. A. Young, L. D. Barke, M. L. Bertrand, M. Böhm-Vélez, S. Destounis, P. Donlan, S. R. Grobmyer, J. Katzen, K. A. Kist, P. T. Lavin, E. V. Makariou, T. M. Parris, K. J. Schilling, F. L. Tucker, and B. E. Dogan, "A Pivotal Study of Optoacoustic Imaging to Diagnose Benign and Malignant Breast Masses: A New Evaluation Tool for Radiologists," *Radiology* **287**(2), 398–412 (2018).
38. M. Yang, L. Zhao, X. He, N. Su, C. Zhao, H. Tang, T. Hong, W. Li, F. Yang, L. Lin, B. Zhang, R. Zhang, Y. Jiang, and C. Li, "Photoacoustic/ultrasound dual imaging of human thyroid cancers: An initial clinical study," *Biomed. Opt. Express* **8**(7), 3449–3457 (2017).
39. J. Kim, M. H. Kim, K. Jo, J. Ha, and C. Kim, "Photoacoustic analysis of thyroid cancer in vivo: a pilot study," *Proc. SPIE* **10064**, 1006408 (2017).
40. K. Irisawa, K. Hirota, A. Hashimoto, M. Dai, H. Ishii, T. Tada, T. Wada, T. Hayakawa, R. Azuma, and N. Otani, "Photoacoustic imaging system for peripheral small-vessel imaging based on clinical ultrasound technology," *Proc. SPIE* **9708**, 970807 (2016).
41. P. Hai, Y. Zhou, J. Liang, C. Li, and L. V. Wang, "Photoacoustic tomography of vascular compliance in humans," *J. Biomed. Opt.* **20**(12), 126008 (2015).
42. Y. Sun, E. Sobel, and H. Jiang, "Quantitative three-dimensional photoacoustic tomography of the finger joints: an in vivo study," *J. Biomed. Opt.* **14**(6), 064002 (2009).
43. N. Huang, M. He, H. Shi, Y. Zhao, M. Lu, X. Zou, L. Yao, H. Jiang, and L. Xi, "Curved-array-based multispectral photoacoustic imaging of human finger joints," *IEEE Trans. Biomed. Eng.* **65**(7), 1452–1459 (2018).
44. A. Taruttis, A. C. Timmermans, P. C. Wouters, M. Kacprowicz, and V. Ntziachristos, "Optoacoustic Imaging of Human Vasculature: Feasibility by Using a Handheld Probe," *Radiology* **281**(1), 256–263 (2016).
45. M. Oeri, W. Bost, N. Sénégon, S. Tretbar, and M. Fournelle, "Hybrid Photoacoustic/Ultrasound Tomograph for Real-Time Finger Imaging," *Ultrasound Med. Biol.* **43**(10), 2200–2212 (2017).
46. S. Ermilov, R. Su, M. Zamora, T. Hernandez, and A. Oraevsky, "Optoacoustic angiography of peripheral vasculature," *Proc. SPIE* **8223**, 82230D (2012).
47. M. Ishihara, A. Horiguchi, H. Shinmoto, H. Tsuda, and T. Asano, "Comparison of transrectal photoacoustic, Doppler, and magnetic resonance imaging for prostate cancer detection," *Proc. SPIE* **9708**, 970852 (2016).
48. S.-R. Kothapalli, G. A. Sonn, J. W. Choe, A. Nikoozadeh, A. Bhuyan, K. K. Park, P. Cristman, R. Fan, A. Moini, B. C. Lee, J. Wu, T. E. Carver, D. Trivedi, L. Shiiba, I. Steinberg, D. M. Huland, M. F. Rasmussen, J. C. Liao, J. D. Brooks, P. T. Khuri-Yakub, and S. S. Gambhir, "Simultaneous transrectal ultrasound and photoacoustic human prostate imaging," *Sci. Transl. Med.* **11**(507), eaav2169 (2019).
49. S. Okawa, K. Sei, T. Hirasawa, K. Irisawa, K. Hirota, T. Wada, T. Kushibiki, K. Furuya, and M. Ishihara, "In vivo photoacoustic imaging of uterine cervical lesion and its image processing based on light propagation in biological medium," *Proc. SPIE* **10064**, 100642S (2017).
50. C. P. Favazza, L. A. Cornelius, and L. V. Wang, "In vivo functional photoacoustic microscopy of cutaneous microvasculature in human skin," *J. Biomed. Opt.* **16**(2), 026004 (2011).
51. A. Karlas, J. Reber, G. Diot, D. Bozhko, and V. Ntziachristos, "Flow-mediated dilatation test using optoacoustic imaging: A proof-of-concept," *Biomed. Opt. Express* **8**(7), 3395–3403 (2017).
52. P. Subochev, A. Orlova, E. Smolina, A. Kirillov, N. Shakhova, and I. Turchin, "Raster-scan optoacoustic angiography reveals 3D microcirculatory changes during cuffed occlusion," *Laser Phys. Lett.* **15**(4), 045602 (2018).
53. M. Xu and L. V. Wang, "Universal back-projection algorithm for photoacoustic computed tomography," *Phys. Rev. E* **71**(1), 016706 (2005).
54. I. Olefir, E. Mercep, N. C. Burton, S. V. Ovsepian, and V. Ntziachristos, "Hybrid multispectral optoacoustic and ultrasound tomography for morphological and physiological brain imaging," *J. Biomed. Opt.* **21**(8), 086005 (2016).
55. X. L. Deán-Ben and D. Razansky, "Functional optoacoustic human angiography with handheld video rate three dimensional scanner," *J. Photoacoust.* **1**(3-4), 68–73 (2013).
56. R. A. De Blasi, M. Ferrari, A. Natali, G. Conti, A. Mega, and G. Gasparetto, "Noninvasive measurement of forearm blood flow and oxygen consumption by near-infrared spectroscopy," *J. Appl. Physiol.* **76**(3), 1388–1393 (1994).
57. R. Klabunde, *Cardiovascular Physiology Concepts* (Lippincott Williams & Wilkins, 2011).
58. T. Tenland, G. Salerud, G. Nilsson, and Å. Öberg, "Spatial and temporal variations in human skin blood flow," *Int. J. Microcirc. Clin. Exp.* **2**(2), 81–90 (1983).

59. Y. Zhu, X. Guan, Y. Jie, J. Janggun, G. Girish, D. Hakan, A. Toshitaka, S. Naoto, S. Yusuke, and W. Xueding, "Light Emitting Diodes based Photoacoustic Imaging and Potential Clinical Applications," *Sci. Rep.* **8**(1), 9885 (2018).
60. M. Xu and L. V. Wang, "Analytic explanation of spatial resolution related to bandwidth and detector aperture size in thermoacoustic or photoacoustic reconstruction," *Phys. Rev. E* **67**(5), 056605 (2003).
61. L. Lin, J. Yao, L. Li, and L. V. Wang, "In vivo photoacoustic tomography of myoglobin oxygen saturation," *J. Biomed. Opt.* **21**(6), 061002 (2015).
62. T. Durduran, R. Choe, W. Baker, and A. G. Yodh, "Diffuse optics for tissue monitoring and tomography," *Rep. Prog. Phys.* **73**(7), 076701 (2010).
63. M. Li, Y. Tang, and J. Yao, "Photoacoustic tomography of blood oxygenation: A mini review," *J. Photoacoust.* **10**, 65–73 (2018).
64. R. Hochuli, L. An, P. C. Beard, and B. T. Cox, "Estimating blood oxygenation from photoacoustic images: can a simple linear spectroscopic inversion ever work?" *J. Biomed. Opt.* **24**(12) 1 (2019)